Dyes and Pigments 190 (2021) 109304

Contents lists available at ScienceDirect

Dyes and Pigments

journal homepage: http://www.elsevier.com/locate/dyepig

Bisquinolinium-fluorescein conjugates as specific fluorescence probes of c-myc Pu22 G-quadruplex and their bioimaging and anticancer activities

Jun-Hui Li [1], Tian-Zhu Ma [1], Jia-Luo Fu, Jun-Tao Huang, Meng-Jia Zhang, Pei-Dan You, Chun-Qiong Zhou [*]

Guangdong Provincial Key Laboratory of New Drug Screening, School of Pharmaceutical Sciences, Southern Medical University, Guangzhou, 510515, PR China

ARTICLE INFO

Keywords:
Bisquinolinium-fluorescein conjugates
C-myc Pu22 G-quadruplex
G-quadruplex probes
Bioimaging
Cell activity

ABSTRACT

Targeting G-quadruplexes in the c-myc gene promoter region is one of the few therapeutic opportunities through inhibiting the c-myc protein overexpression. However, the design of probes recognizing c-myc G-quadruplexes with high selectivity and specificity and the more evaluation of cellular system still remain a big challenge. Here, two novel bisquinolinium-fluorescein conjugates (**1a** and **1b**) with the alkyl linkers, have been designed and evaluated their selectivity and specificity for parallel c-myc Pu22 G-quadruplex. Compared with conjugate **1b** with longer alkyl linker, conjugate **1a** with shorter alkyl linker, exhibited higher fluorescence response and specificity towards c-myc Pu22 G-quadruplex than other wild-type c-myc G-quadruplexes, human telomere G-quadruplexes, other G-quadruplexes in the promoter regions and double-stranded DNA. According to the binding mode, the interaction of compound **1a** with the 2nd loop around the 3′-end G-quartet through regulating the length of the alkyl linker, excited its fluorescence and enhanced its selectivity towards c-myc Pu22 G-quadruplex. Furthermore, conjugate **1a** could selectively recognize c-myc Pu22 G-quadruplex DNA in cells through microscopy experiments, and inhibit cell proliferation possibly by reducing c-myc protein expression in cancer cells. This study provides guidance to design the high-performance fluorescence probes towards c-myc G-quadrulex by regulating the alkyl linker in the conjugate of G-quadruplex binder and fluorescence ligand, and develop anticancer drugs targeting c-myc G-quadruplex.

1. Introduction

G-quadruplex nucleic acids widely exist in human telomere and the promoter regions of genes, and play the important biological roles in oncogene transcription regulation, DNA replication and telomere stability [1–6]. In them, one important G-quadruplex sequence found in the nuclease hypersensitive element $NHEIII_1$ is present in the P1 promoter of the c-myc oncogene [7]. The expression of c-myc is upregulated in 70% of different cancer types [8], and 90% of c-myc expression is regulated by G-quadruplexes in $NHEIII_1$ region of the c-myc gene [9]. And the c-myc protein is a transcription factor regulating cellular proliferation, differentiation and apoptosis [10]. So targeting the G-quadruplexes in the promoter region of the c-myc gene is one of the few therapeutic opportunities by controlling the overexpression of the c-myc protein and the transcription of the c-myc oncogene [11].

Then, a great quantity of G-quadruplex binders, such as transition metal [Ru(II), Pt(II) and Ir(III)] complexes [12–16], synthetic fused-ring (quindoline, porphyrin, acridine and benzoxazinone) derivatives [17–21], and natural products (carbamide, Fonsecin B and flavonoid quercetin) [22,23] have been reported to bind and stabilize c-myc G-quadruplex. However, most binders have not been further evaluated their potential anticancer activities and possible action mechanism [18,24]. On the other hand, some fluorescence probes have been reported to display high visualization towards c-myc G-quadruplex [25–29]. But most G-quadruplex probes exhibited poor selectivity towards c-myc G-quadruplex for only interacting with G-quadruplexes by generic G-quatet stacking. Interacting with the flanking loops around the G-quartet has become an excellent way to increase the selectivity of the probes towards c-myc G-quadruplex [27,30]. In addition, the selectivity of fluorescent probes towards c-myc G-quadruplex could be increased by conjugating a recognition group and a fluorescent signalling unit with a flexible chain. Though these probes with selectivity and specificity

* Corresponding author.
E-mail address: huagongzhoucq@163.com (C.-Q. Zhou).
[1] These authors contributed equally.

https://doi.org/10.1016/j.dyepig.2021.109304
Received 5 January 2021; Received in revised form 9 March 2021; Accepted 10 March 2021
Available online 16 March 2021

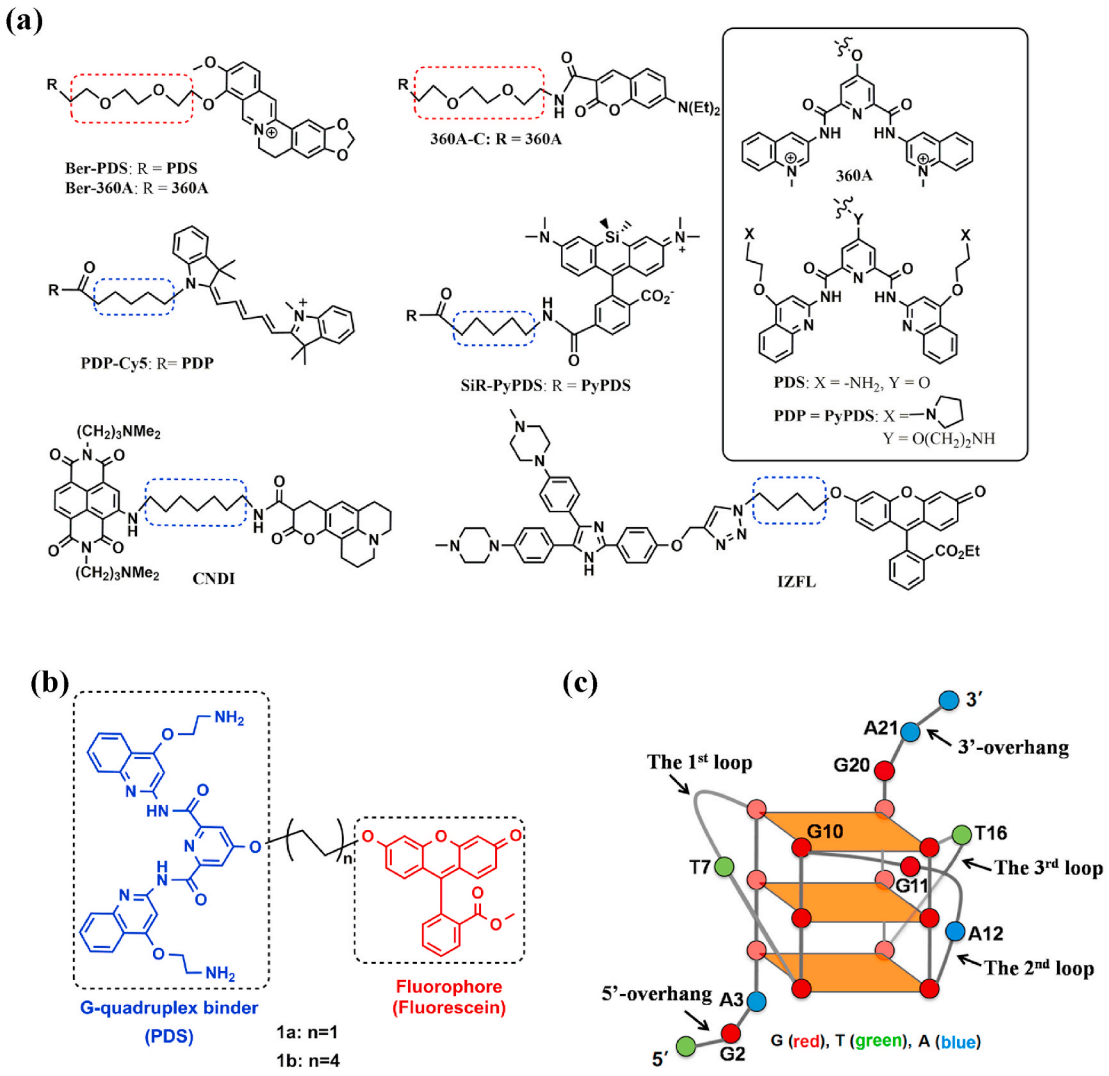

Scheme 1. (a) Structures of the reported probes linking G-quadruplex binder and fluorophore ligand with polyether or alkyl linker. (b) Structures of conjugates **1a** and **1b**. (c) Structure model of wild-type c-myc pu22 G-quadruplex.

towards c-myc G-quadruplex have been reported, they still have some deficiencies in either selectivity towards c-myc G-quadruplex or the evaluation of cellular system [31–36]. Thus, the design of these conjugates with high-performance in vitro and in vivo is still one of the major challenges in the field.

Over a few years ago, our group have reported some fluorescence probes targeting G-quadruplexes [37–39]. Through the regulation of the polyether linker length between two fluorescent signalling units, these berberine dimers showed excellent fluorescence response towards hybrid-type and antiparallel dimeric G-quadruplexes [37,38]. Especially, two berberine-bisquinolinium conjugates (**Ber- PDS** and **Ber-360A**, Scheme 1a) by linking the fluorophore ligand and the G-quadruplex binder with the polyether chain have showed high selectivity and sensitivity towards hybrid-type and antiparallel dimeric G-quadruplexes and excellent bioimaging towards G-quadruplexes in cells [39]. And the conjugate **360A-C** with polyether chain (Scheme 1a) has also showed high fluorescence response towards hybrid-type and antiparallel G-quadruplexes [34]. Here, conjugates will be expected to target parallel c-myc G-quadruplex. Some conjugates with the alkyl linkers (such as **PDP-Cy5**, **SiR-PyPDS**, **IZFL** and **CNDI**, Scheme 1a) have been reported to fluorescently recognize parallel G-quadruplexes, especially c-myc [35,36,40,41]. Thus, we have designed two bisquinolinium-fluorescein conjugates **1a** and **1b** (Scheme 1b) linked with different-length alkyl linkers. On base of bisquinolinium derivative—pyridostatin (**PDS**) as an excellent c-myc G-quadruplex stabilizer [42] and a potential cancer therapeutic agent [43,44], the bisquinolinium-fluorescein conjugates with the alkyl linkers will be expected to target parallel c-myc G-quadruplex. In addition, through regulating the length of the alkyl linker, the fluorescein section will be expected to interact with the flanking loops around the G-quartet, enhance the selectivity and result in fluorescence detection for c-myc G-quadruplex [27,30]. Their binding affinity, thermal stabilization, selectivity and visualization towards c-myc G-quadruplex in vitro will be discussed. And their visualization in cells, cancer cell cytotoxicity and inhibition of c-myc expression will also further be studied.

2. Experimental section

2.1. General

NMR (^{1}H and ^{13}C) and MS (ESI and HR) spectra were recorded on a Bruker Avance 400 MHz Ultrashield NMR spectrometer and a LCT Premier mass spectrophotometer, respectively. All chemicals were purchased from Sigma-Aldrich, BDH, or Apollo Scientific and used without further purification. Compounds **1a** and **1b** were dissolved in DMSO solution to give 10 mM stock solution, diluted to 1 mM with DMSO before use, and then further diluted using suitable buffer to the appropriate concentration. Oligonucleotides (Tables 1 and 2) from

Table 1
DNA strands used in the paper.

DNA	Sequence (from 5′ to 3′)	Structure
Pu18	$AG_3TG_4AG_3TG_4$	Paral G1[a]
Pu22	$TGAG_3TG_4AG_3TG_4AA$	Paral G1
Pu24	$TGAG_3TG_4AG_3TG_4AAGG$	Paral G1
Pu27	$TG_4AG_3TG_4AG_3TG_4AAGG$	Paral G1
Telo22 (K^+)	$AGGG(TTAGGG)_3$	Hybrid[b] G1
Telo22 (Na^+)	$AGGG(TTAGGG)_3$	Anti[c] G1
G2T1 (K^+)	$AGGG(TTAGGG)_7$	Hybrid G2T1[d]
G2T1 (Na^+)	$AGGG(TTAGGG)_7$	Anti G2T1
c-kit1	$G_3AG_3CGCTG_3AG_2AG_3$	Paral G1
c-kit2	$G_3CG_3(CG)_2(AG_3)_2G$	Paral G1
VEGF	$CG_4CG_3CCG_5CG_4T$	Paral G1
KRAS	$AG_3CGGTGTG_3AAGAG_3AAGAG_5AGG$	Paral G1
bcL-2	$G_3CG_3CGCG_3AGGAAG_5CG_3$	Paral G1
5′-Cy5-Pu22	5′-Cy5-$TGAG_3TG_4AG_3TG_4AA$	Paral G1
5′-Cy5-c-kit1	5′-Cy5-$G_3AG_3CGCTG_3AG_2AG_3$	Paral G1
5′-Cy5-Telo22	5′-Cy5-$AGGG(TTAGGG)_3$	Paral G1
ds 26	CAATCGGATCGAATTCGATCCGATTG + GTTAGCCTAGCTTAAGCTAGGCTAAC	Double-stranded
CT DNA		Double-stranded

[a] Paral = Parallel, G1 = monomeric G-quadruplex.
[b] Hybrid = Hybrid-type, the DNA sequences of Telo22 and G2T1 in K^+ buffer formed hybrid-type G-quadruplexes.
[c] Anti = Antiparallel, the DNA sequences of Telo22 and G2T1 in Na^+ buffer formed antiparallel G-quadruplexes.
[d] G2T1 = dimeric G-quadruplex.

Table 2
The mutants of Pu22 G-quadruplexes in the binding site analysis.

Name	Sequence (from 5′ to 3′)
Pu22-G2>C2	T**C**AGGGTGGGGAGGGTGGGGAA
Pu22-A3>T3	TG**T**GGGTGGGGAGGGTGGGGAA
Pu22-T7>A7	TGAGGG**A**GGGGAGGGTGGGGAA
Pu22-G10>C10	TGAGGGTGG**C**GAGGGTGGGGAA
Pu22-G11>C11	TGAGGGTGGG**C**AGGGTGGGGAA
Pu22-A12>T12	TGAGGGTGGGG**T**GGGTGGGGAA
Pu22-T16>A16	TGAGGGTGGGGAGGG**A**GGGGAA
Pu22-G20>C20	TGAGGGTGGGGAGGGTGGG**C**AA
Pu22-A21>T21	TGAGGGTGGTTAGGGTGGGG**T**A

Shanghai Sangon Biological Engineering Technology & Services (Shanghai, China) were dissolved in suitable buffer. The G-rich DNA sequences were annealed by heating to 95 °C for 10 min and then cooled to room temperature overnight.

2.2. Synthesis

2.2.1. Synthesis of 6-((8-bromooctyl)oxy)-9-(2-propionylphenyl)-3H-xanthen-3-one (4b)

Compound **2** (600 mg, 1.70 mmol) was mixed with K_2CO_3 (480 mg, 3.50 mmol) and 1, 8-dibromooctane (1.7 g, 9.15 mmol) in DMF (40 mL), and the resulting reaction mixture was refluxed for 2 h and cooled to room temperature. The reaction solution was evaporated under reduced pressure and purified by chromatography on a silica gel column, eluting with cyclohexane/$CH_3COOCH_2CH_3$ (1/1, v/v), to afford compound **4b** (220 mg, 70%) as a red solid, having ^{1}H NMR (400 MHz, DMSO-d_6) δ 8.22 (d, J = 7.6 Hz, 1H),7.88 (t, J = 7.2 Hz, 1H), 7.79 (t, J = 7.6 Hz, 1H), 7.50 (d, J = 7.6 Hz, 1H), 7.22 (d, J = 2.0 Hz, 1H), 6.89 (dd, J = 9.0 Hz, J = 1.8 Hz, 1H), 6.83 (d, J = 8.0 Hz, 1H), 6.80 (d, J = 12.0 Hz, 1H), 6.39 (dd, J = 9.8 Hz, J = 1.4 Hz, 1H), 6.24 (d, J = 1.2 Hz, 1H), 4.14 (t, J = 6.4 Hz, 1H), 3.59 (s, 3H), 3.53 (t, J = 6.4 Hz, 2H), 1.84–1.72 (m, 4H), 1.41–1.38 (m, 4H), 1.33–1.30 (m, 4H). ^{13}C NMR (100 MHz, DMSO-d_6) δ 183.3, 165.6, 164.2, 158.8, 154.4, 134.2, 133.6, 131.1, 131.0, 130.9, 130.5, 129.9, 129.5, 129.1, 117.0, 114.8, 114.7, 104.8, 101.3, 69.2, 52.7, 35.5, 32.6, 28.9, 28.7, 28.4, 27.9, 25.7. ESI-MS: *m/z* 537.07 ($[M+H]^+$) and HR-MS for $C_{29}H_{29}O_5Br$ ($[M+H]^+$) calcd: 537.1271, found: 537.1277.

2.2.2. Synthesis of Methyl2-(6-(2-((2,6-bis((4-(2-((tert-butoxycarbonyl) amino)ethoxy) quinolin-2-yl)carbamoyl)pyridin-4-yl)oxy)ethoxy)-3-oxo-3H-xanthen-9-yl)benzoate (6a)

Compound **5** (75 mg, 0.1 mmol) was mixed with K_2CO_3 (28 mg, 0.2 mmol), compound **4a** (69 mg, 0.2 mmol) and KI (8 mg, 0.05 mmol) in DMF (1 mL), and the resulting reaction mixture was heated for 4 h at 60 °C and cooled to room temperature. The mixture was then poured into water and filtrated to obtain the crude product which was purified by chromatography on a silica gel column, eluting with DCM/CH_3OH (40/1, v/v), to afford compound **6a** (62 mg, 55%) as an orange-yellow solid, having ^{1}H NMR (400 MHz, DMSO-d_6) δ 12.04 (s, 2H),8.24 (s, 1H), 8.22 (d, J = 7.6 Hz, 2H), 8.06 (s, 2H), 7.99 (s, 2H), 7.94 (d, J = 8.0 Hz, 2H), 7.88 (t, J = 8.0 Hz, 1H), 7.80 (d, J = 6.8 Hz, 1H), 7.77 (t, J = 8.0 Hz, 2H), 7.53 (s, 1H), 7.50 (d, J = 8.4 Hz, 2H), 7.35 (s, 1H), 7.20 (t, J = 5.4 Hz, 2H), 6.97 (d, J = 9.2 Hz, 1H), 6.86 (d, J = 8.8 Hz, 1H), 6.81 (d, J = 8.0 Hz, 1H), 6.40 (d, J = 9.6 Hz, 1H), 6.26 (s, 1H), 4.74 (s, 2H), 4.63 (s, 2H), 4.27 (s, 4H), 3.60 (s, 3H), 3.55 (m, 2H), 3.54 (m, 2H),1.41 (s, 18H). ^{13}C NMR (100 MHz, DMSO-d_6) δ 184.3, 167.4, 165.6, 163.6, 163.1, 162.6, 158.8, 156.3, 153.9, 152.8, 151.5, 150.3, 147.4, 134.3, 133.6, 131.1, 131.0, 130.8, 130.5, 129.9, 129.8, 129.3, 127.2, 124.8, 122.6, 119.6, 117.2, 115.0, 114.4, 112.6, 105.0, 101.7, 95.3, 78.3, 68.2, 52.7, 29.7, 28.6. ESI-MS: *m/z* 1126.29 ($[M+H]^+$) and HR-MS for $C_{62}H_{59}N_7O_{14}$ ($[M+H]^+$) calcd: 1126.4193, found: 1126.4180.

2.2.3. Synthesis of Methyl 2-(6-((8-((2,6-bis((4-(2-((tert-butoxycarbonyl) amino) ethoxy)quinolin-2-yl)carbamoyl)pyridin-4-yl)oxy)octyl)oxy)-3-oxo-3H-xanthen-9-yl)benzoate (6b)

Compound **6b** was prepared following the same procedure as the one described for compound **6a**. The following amounts were used: compound **5** (38 mg, 0.06 mmol), K_2CO_3 (15 mg, 0.1 mmol), compound **4b** (60 mg, 0.11 mmol) and KI (9 mg, 0.05 mmol). Yield: 30 mg (50%) as an orange-yellow solid. ^{1}H NMR (400 MHz, DMSO-d_6) δ 11.97 (s, 2H), 8.24 (s, 1H), 8.21 (d, J = 10.0 Hz, 2H), 8.04 (s, 2H), 7.92 (d, J = 8.8 Hz, 2H), 7.89 (s, 2H), 7.85 (d, J = 7.2 Hz, 1H), 7.78 (s, 1H), 7.75 (d, J = 6.0 Hz, 2H), 7.51 (d, J = 8.0 Hz,1H), 7.49 (d, J = 6.4 Hz, 2H), 7.20 (s, 1H), 7.19 (s, 2H), 6.85 (s, 1H), 6.80 (d, J = 7.2 Hz, 1H), 6.75 (d, J = 10.0 Hz, 1H), 6.34 (d, J = 9.6 Hz, 1H), 6.21 (s, 1H), 4.29 (s, 2H), 4.26 (s, 4H), 4.14 (s, 2H), 3.59 (s, 3H), 3.54 (br, 4H), 1.82 (s, 2H), 1.77 (s, 2H), 1.46 (s, 4H), 1.41 (br, 22H). ^{13}C NMR (100 MHz, DMSO-d_6) δ 184.2, 167.7, 165.7, 163.8, 163.7, 162.6, 158.8, 156.3, 154.0, 152.9, 151.5, 150.5, 147.5, 134.4, 133.6, 131.1, 131.0, 130.0, 129.2, 127.2, 119.7, 117.0, 114.6, 114.3, 112.4, 105.0, 101.3, 95.3, 78.3, 69.1, 68.2, 52.8, 29.0, 28.7, 25.8. ESI-MS: *m/z* 1210.11 ($[M+H]^+$) and HR-MS for $C_{68}H_{71}N_7O_{14}$ ($[M+2H]^{2+}$) calcd: 605.7602, found: 605.7601.

2.2.4. Synthesis of Methyl 2-(6-(2-((2,6-bis((4-(2-aminoethoxy)quinolin-2-yl) carbamoyl)pyridin-4-yl)oxy)ethoxy)-3-oxo-3H-xanthen-9-yl) benzoate(1a)

Compound **6a**(42 mg, 0.04 mmol)was mixed with CF_3COOH (1.0 mL) in DCM (2.0 mL). The resulting reaction mixture was stirred at room temperature for 1 h, then concentrated under reduced pressure and afforded compound **1a** (35 mg, 98%) as an orange-yellow solid, having ^{1}H NMR (400 MHz, DMSO-d_6) δ 12.10 (s, 2H), 8.45 (d, J = 8.0 Hz, 2H), 8.23 (d, J = 8.0 Hz, 2H), 8.12 (s, 1H), 8.00 (s, 2H), 7.96 (d, J = 8.0 Hz, 2H), 7.89 (t, J = 7.6 Hz, 1H), 7.83 (s, 1H), 7.80 (d, J = 6.8 Hz, 2H), 7.57 (d, J = 7.6Hz, 1H), 7.53 (t, J = 6.4 Hz, 2H), 7.40 (s, 1H), 7.00 (d, J = 8.8 Hz, 1H), 6.93 (d, J = 3.6 Hz,1H), 6.85–6.89 (br, 1H), 6.47 (t, J = 5.2 Hz,1H), 6.35 (d, J = 10.4 Hz, 1H), 4.75 (br, 2H), 4.66 (br, 2H), 4.52 (br, 4H), 3.60 (s, 3H), 3.48 (br, 4H). ^{13}C NMR (100 MHz, DMSO-d_6) δ 167.4, 165.6, 163.7, 163.5, 162.1, 158.8, 158.6, 152.7, 151.5, 150.6, 147.6, 134.2, 133.7, 131.3, 131.2, 131.1, 130.6, 127.1, 124.9, 123.1, 119.4, 117.3, 115.2, 112.7, 111.8, 101.7, 95.4, 65.6, 52.7, 38.6. ESI-MS: *m/z* 926.22 ($[M+H]^+$) and HR-MS for $C_{52}H_{43}N_7O_{10}$ ($[M+H]^+$) calcd: 926.3144, found: 926.3145.

*2.2.5. Synthesis of Methyl2-(6-((8-((2,6-bis((4-(2-aminoethoxy)quinolin-2-yl) carbamoyl)pyridin-4-yl)oxy)octyl)oxy)-3-oxo-3H-xanthen-9-yl) benzoate **(1b)***

Compound **1b** was prepared following the same procedure as the one described for compound **1a**. The following amounts were used: compound **6b** (30 mg, 0.025 mmol) and CF_3COOH (1.0 mL). Yield: 25 mg (98%) as an orange-yellow solid. ^{1}H NMR (400 MHz, DMSO-d_6) δ 12.05 (s, 2H), 8.44 (d, J = 8.4 Hz, 2H), 8.23 (d, J = 8.0 Hz, 2H), 8.11 (s, 1H), 7.95 (d, J = 8.4 Hz, 2H), 7.93 (s, 2H), 7.88 (d, J = 7.2 Hz, 1H), 7.82 (s, 1H), 7.79 (t, J = 6.8 Hz, 2H), 7.56 (t, J = 7.2 Hz, 2H), 7.51 (d, J = 7.6 Hz, 1H), 7.30 (s, 1H), 6.93 (d, J = 4.8 Hz, 1H), 6.88 (d, J = 9.6 Hz, 1H), 6.49 (d, J = 9.6 Hz, 1H), 6.42 (s, 1H), 4.51 (t, J = 4.0 Hz, 4H), 4.32 (t, J = 6.4 Hz, 2H), 4.19 (t, J = 6.0 Hz, 2H), 3.58 (s, 3H), 3.49 (d, J = 4.4 Hz, 4H), 1.77–1.86 (br, 4H), 1.48 (s, 4H), 1.41 (s, 4H). ^{13}C NMR (100 MHz, DMSO-d_6) δ 167.7, 165.6, 163.7, 162.1, 158.9, 152.7, 151.4, 147.4, 133.6, 131.2, 131.1, 131.0, 130.6, 129.8, 129.7, 127.1, 124.9, 123.1, 119.4, 117.0, 115.3, 112.5, 104.6, 101.3, 95.4, 69.4, 69.2, 65.6, 52.8, 38.6, 28.9, 28.7, 28.5, 25.7, 25.6. ESI-MS: *m/z* 1010.38 ($[M+H]^+$), 505.79 ($[M+2H]^{2+}$) and HR-MS for $C_{58}H_{55}N_7O_{10}$ ($[M+2H]^{2+}$) calcd: 505.7078, found: 505.7082.

2.3. Fluorescence spectra studies

Compounds **1a** and **1b** (1 μM or 2 μM) were added into concentrate solutions of oligonucleotides in suitable buffer. The fluorescence data were collected at $\lambda_{ex}/\lambda_{em}$ = 455/516 nm. The fluorescence data were analyzed to give the apparent binding constants (K_a) of **1a** and **1b** towards different DNA sequences by non-linear fitting [38,39,45]. Fluorescence competition titrations of the conjugate towards Pu22 with double-stranded DNA (such as ds 26 and CT DNA) were performed by fixing the concentration of conjugate **1a** and double-stranded DNA with increasing concentration of Pu22. They were also measured by keeping the concentration of the conjugate and Pu22 with increasing concentration of double-stranded DNA. The solutions were prepared in 10 mM Tris-HCl buffer (5 mM KCl, 95 mM LiCl and pH 7.2) and measured at $\lambda_{ex}/\lambda_{em}$ = 455/516 nm.

The quantum yield values (Φ_F) of conjugate (2 μM) with different DNA (G2T1: 2 μM; G1 and ds 26: 8 μM; CT DNA: 200 μM (base concentration)) were measured according to the experimental method from the reported literature and calculated relative to a standard solution of fluorescein in 0.1 mol/L NaOH water (Φ_s = 0.90, λ_{ex} = 490 nm) [46]. The detection limit was calculated according to the equation $3\sigma_{bi}/m$, wherein σ_{bi} is the standard deviation of blank measurements, and m is the slope of the straight line between the fluorescence intensity of compounds **1a** and **1b** (1 μM) in the absence of Pu22 G-quadruplex and the concentration of **1a** and **1b** [38,39].

2.4. UV–Vis titration

UV–Vis spectra were measured by maintaining the concentration of the conjugate (**1a**/**1b**) with increasing the concentration of Pu22 in 10 mM Tris-HCl buffer (5 mM KCl, 95 mM LiCl and pH 7.2) at room temperature.

2.5. CD procedures

CD spectra were measured on annealed Pu22 (5.0 μM) in 10 mM Tris-HCl (5 mM KCl, 95 mM LiCl and pH 7.2) with compound **1a** or **1b**, and nonannealed Pu22 (5.0 μM) in 10 mM Tris-HCl (pH 7.2) with compound **1a** or **1b**. CD-melting assays of different DNA sequences in 10 mM Tris-HCl buffer with different K^+ or Na^+ concentration (5 mM KCl and 95 mM LiCl for Pu22, 10 mM KCl and 90 mM LiCl for c-kit1, VEGF, KRAS and bcL-2, 20 mM KCl and 80 mM LiCl for c-kit2, 100 mM KCl for ds 26 and hybrid-type G2T1 and Telo22, and 100 mM NaCl for antiparallel G2T1 and Telo22) were performed without or with compounds **1a** and **1b**. The experimental condition is the 100 nm/min scanning speed, the 2 s response time and the 1 °C/min heating rate. The melting temperature (T_m) was calculated from the melting profiles with the software origin 8.0.

2.6. Gel electrophoresis

Native gel electrophoresis was carried out on acrylamide gel (15%), and run at 0 °C in 1 × TBE buffer (pH 8.3). The first gel was obtained with DNA samples, and the run gel was stained by Gel red. The second gel was obtained with DNA samples in 10 mM Tris-HCl buffer (100 mM KCl for ds 26 and hybrid-type G2T1 and Telo22, 10 mM KCl and 90 mM LiCl for c-kit1, VEGF, KRAS and bcL-2, 20 mM KCl and 80 mM LiCl for c-kit2, and 5 mM KCl and 95 mM LiCl for Pu22) premixed with compound **1a**, and this run gel need not be stained by Gel red [30]. The fluorescence recognition of compound **1a** towards Pu22 was analyzed using Alpha Hp 3400 fluorescence and visible-light digitized image analyzer.

2.7. Molecular modelling

The molecule structure of compounds **1a** and **1b** were constructed and optimized using Molecular Operating Environment (MOE) package, while the three-dimensional structure of G-quadruplex was constructed and optimized by the Chimera package [47]. The initial structures of G-quadruplex with compound **1a** and **1b** were manually built by molecular docking in MOE to give the binding energies [48]. The visual analysis of binding modes was obtained in force field by Python molecule (PyMOL).

2.8. Confocal imaging of co-localization

MCF-7 and A549 cells were cultured in Dulbecco's modified Eagle's medium (Gibco) with 1% glutamine and 10% fetal bovine serum (FBS) for 24 h at 37 °C. 40 pmol annealed 5′-Cy5-Pu22, 5′-Cy5-c-kit1 and 5′-Cy5-Telo22 G-quadruplexes (Table 1) were transfected into cells by using lipofectamine 2000 (Thermo Fisher) and incubated at 37 °C for 5 h. Then compound **1a** (5 μM) was added and incubated for another 2 h. The digital images were recorded using a confocal laser scanning microscopy (Olympus FV1000-MP). The location of compound **1a** was investigated by the fluorescence signal collected between 500 and 570 nm at λ_{ex} = 455 nm, and the location of G-quadruplexes were checked by fluorescence signal collected between 655 and 755 nm at λ_{ex} = 635 nm [30].

2.9. Assay of cytotoxicity

Antitumor activities of compounds **1a** and **1b** were measured against three cancer cells (A549,MCF-7 and HeLa) by MTT assay [39].

2.10. Western blot experiments

A549 cells were treated with compounds **1a** and **1b** at 0, 10, 20, 40 and 60 μM for 24 h at 37 °C in a humidified CO_2 incubator. After the incubation period, lysed with extraction buffer and centrifuged to harvest the supernatant. After the protein concentration was calculated with a BCA protein assay kit (Thermo Fisher Scientific), an equal amount of protein (20 μg) was electrophoresed on a 10% SDS−PAGE gel and transferred to a nitrocellulose membrane at 250 mA for 2h. After the membranes were blocked for 1 h with a 5% nonfat dry milk solution in TBS containing 1% Tween-20 at room temperature, membranes with the samples were firstly incubated overnight at 4 °C with primary antibodies, then incubated with the secondary antibodies at room temperature for 2 h. Finally, the c-myc and GAPDH bands were visualized on X-ray film using an enhanced chemiluminescence system (Tron). Relative band intensities were determined by using ImageJ software [14,27,49]. The experiments were repeated three times. The data were expressed as the mean ± SEM.

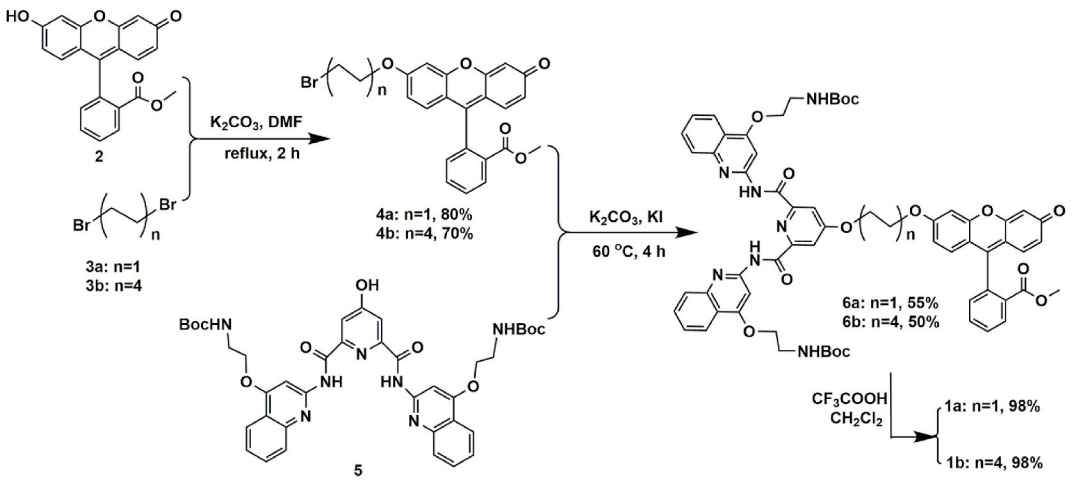

Scheme 2. Synthetic route of conjugates **1a** and **1b**.

3. Results and discussion

3.1. Synthesis of bisquinolinium-fluorescein conjugates

The synthetic route of bisquinolinium-fluorescein conjugates **1a** and **1b** is shown in Scheme 2. Compound **2** was mixed with 1, 8-dibromooctane and K_2CO_3 in DMF. The mixture was refluxed for 2 h and obtained compound **4b** in 70% yield. Compound **5** was added into compound **4a** or **4b** with K_2CO_3 and KI in DMF. The mixtures were heated for 4 h at 60 °C and afforded compounds **6a∼b** in 55 and 50% yield, respectively. Compounds **6a∼b** were then deprotected with trifluoroacetic in dichloromethane and afforded conjugates **1a∼b** in 98 and 96% yield, respectively. Compounds **4b**, **6a∼b** and **1a∼b** were fully characterized on the basis of NMR spectroscopy (^{1}H and ^{13}C) and mass spectrometry (LR and HR) (seeing supplementary material, Figs. S1–15). Compounds **2, 4a** and **5** were prepared according to reported references [36,39,50].

3.2. Spectroscopic recognition towards DNA

Firstly, we screened the fluorescence responses of compounds **1a** and **1b** towards a wide range of DNA sequences, including hybrid-type G2T1 and Telo22, antiparallel G2T1 and Telo22, c-myc Pu22, c-kit1, c-kit2, VEGF, KRAS, bcL-2, ds 26 and CT DNA. Compound **1a** was essentially non-fluorescent, and addition of hybrid-type G2T1 and Telo22, antiparallel G2T1 and Telo22, c-kit1, c-kit2, VEGF, KRAS, bcL-2, ds 26 and CT DNA induced weak changes in the fluorescence intensity (Fig. S17a).

Table 3
Relative fluorescence intensities (F/F_0), binding constants (K_a, μM^{-1}) of compound **1a** with different DNA sequences by fluorimetric titrations, and thermal stabilization (ΔT_m, °C) of different DNA sequences with compound **1a** by CD-melting.

DNA	F/F_0	K_a	ΔT_m
Pu22	25	6.31 ± 0.84	16.1 ± 0.4
G2T1 (Na^+)	6.7	1.00 ± 0.31	−0.1 ± 0.1
G2T1 (K^+)	4.2	1.02 ± 0.26	4.6 ± 0.3
Telo22 (Na^+)	3.9	1.24 ± 0.28	−0.4 ± 0.1
Telo22 (K^+)	3.4	0.27 ± 0.07	−4.0 ± 0.5
c-kit1	4.2	1.02 ± 0.41	−2.1 ± 0.3
c-kit2	3.4	0.22 ± 0.09	−7.1 ± 0.5
VEGF	4.1	1.68 ± 0.45	2.8 ± 0.2
KRAS	3.7	1.32 ± 0.47	ND [a]
bcL-2	4.5	1.00 ± 0.23	1.1 ± 0.2
ds 26	1.6	0.081 ± 0.005 [b]	−0.2 ± 0.1

[a] ND denotes that the ΔT_m value could not be detected for the T_m value of KRAS is more than 95 °C.
[b] The values of K_a was measured by UV–Vis titration in Fig. S24a [51].

However, c-myc Pu22 G-quadruplex caused up to 25-fold fluorescence enhancement with a strong new emission peak at $\lambda_{ex}/\lambda_{em} = 455/516$ nm (Figs. S16 and 17a, and Table 3), and dramatic fluorescent colour change from dark to yellow-green (inset of Fig. 1a). Furthermore, we found that the K^+ concentration exhibited a significant impact towards fluorescence response of compound **1a** towards Pu22 (Fig. 1b and S18a). It can be found that c-myc Pu22 G-quadruplex caused up to more than 15-fold fluorescence enhancement when the K^+ concentration was below 20 mM. When the K^+ concentration was equal to 5 mM, compound **1a** showed the strongest fluorescence response towards Pu22. But compound **1a** towards the other G-quadruplexes (c-kit1, c-kit2, VEGF, KRAS and bcL-2, respectively) in gene promoter region still showed weak fluorescence change when the K^+ concentration changed from 100 mM to 10 mM or 20 mM (Fig. S18b). Furthermore, though compound **1a** showed excellent fluorescent response towards Pu22, it did not yield remarkable fluorescence response for other wild-type c-myc G-quadruplexes (Pu18, Pu24 and Pu27) (Fig. 1c). So these results indicate that compound **1a** showed strongest fluorescence response toward c-myc Pu22 G-quadruplex in 10 mM Tris-HCl, 5 mM KCl and 95 mM LiCl buffer. As a comparative study, compound **1b** with a longer alkyl linker towards all DNA sequences exhibited weak changes in the fluorescence intensity (Fig. S17b).

The photochemical and sensing properties of conjugates **1a** and **1b** have further been investigated with the above-mentioned DNA sequences (Fig. 1a). In Tris-HCl buffer, conjugates **1a** and **1b** exhibited low quantum yields (0.02 and 0.03, respectively). In the presences of different DNA sequences, conjugate **1a** exhibited the highest quantum yield ($\Phi_F = 0.67$) towards parallel Pu22, and *ca.* 5.6-fold higher than conjugate **1b** ($\Phi_F = 0.12$). The quantum yield of **1a** for Pu22 was *ca.* 4.8-fold higher than those for antiparallel Telo22 and G2T1, and 9.6 and 22.3-fold higher than those for hybrid-type Telo22 and G2T1. The quantum yield of **1a** for Pu22 was *ca.* 3.9–6.7-fold higher than those for other parallel G-quadruplexes including c-kit1, c-kit2, VEGF, KRAS and bcL-2, and 167-fold higher than those for ds 26 and CT DNA, respectively. Furthermore, the detection limit of **1a** towards Pu22 (0.77 nM) was *ca.* 7.1-fold lower than that of **1b** (5.46 nM) (Fig. S19).

In addition, due to the existence of a large amount of double-stranded DNA in vivo, fluorescence competition recognition will be significant towards Pu22 over double-stranded DNA. As shown in Fig. 1d, S20a and S20b, addition of Pu22 to a mixture of conjugate **1a** and a high concentration of ds 26 or CT DNA, resulted in comparable fluorescence responses to the case without double-stranded DNA. In contrast, addition of ds 26 or CT DNA (Figs. S20c and S20d) had no remarkable effect on the fluorescence response of conjugate **1a** for Pu22. These results indicate that conjugate **1a** could still selectively recognize Pu22 in the presence of a large amount of double-stranded DNA.

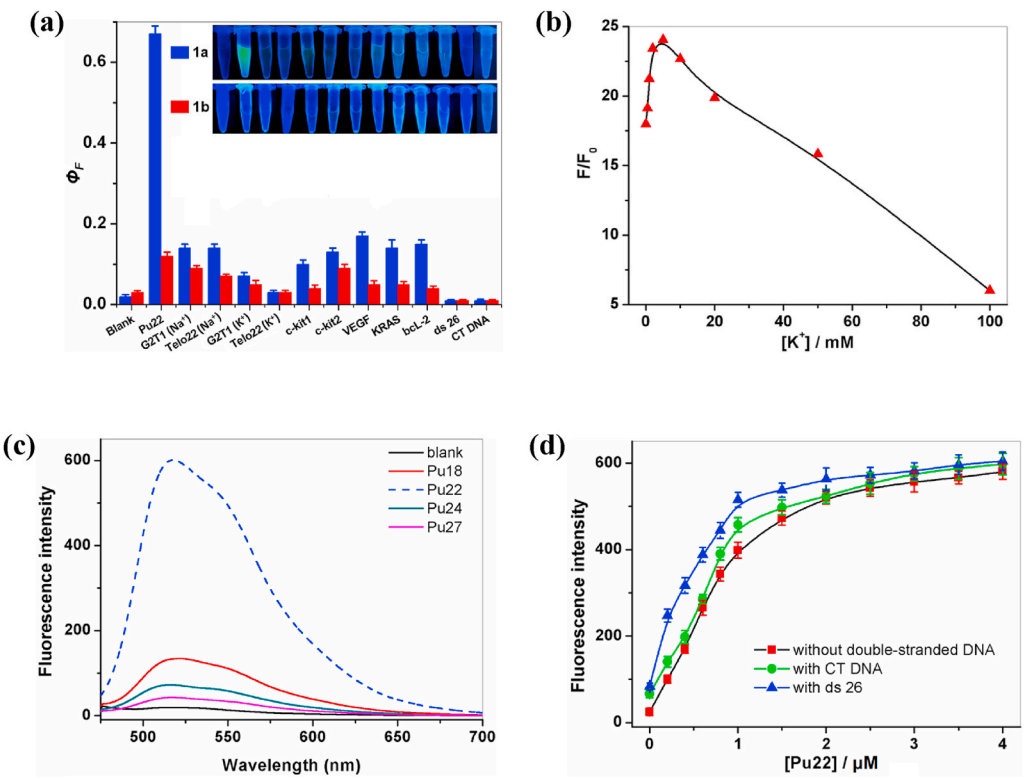

Fig. 1. (a) Fluorescence quantum yields (Φ_F) of two compounds (2 μM) without and with different DNA (G2T1: 2 μM; G1 and ds 26: 8 μM; CT DNA: 200 μM (base concentration)). Inset: colour change of compounds **1a** and **1b** in the presence of different DNA sequences. (b) Plot of F/F_0 at 516 nm *vs* $[K^+]$ on compound **1a** (1 μM) and Pu22 (4 μM) in 10 mM Tris-HCl buffer with different K^+ concentrations (0–100 mM) and $[K^+] + [Li^+] = 100$ mM. (c) Fluorescence intensities of compound **1a** (1 μM) in the presence of 4 μM Pu22 and wild-type c-myc (Pu18, Pu24 and Pu27, respectively) in 10 mM Tris-HCl buffer (5 mM KCl, 95 mM LiCl and pH 7.2). (d) Fluorescence intensities of conjugate **1a** (1 μM) with addition of Pu22 (0–4 μM) in the absence and presence of double-stranded DNA (ds 26: 8 μM, CT DNA: 200 μM (base concentration)). $\lambda_{ex}/\lambda_{em}$ = 455/516 nm.

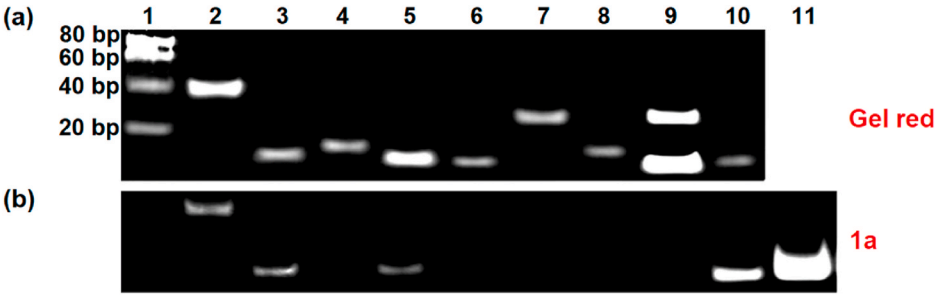

Fig. 2. Electrophoresis of DNA oligonucleotides on 15% nondenaturing acrylamide gel stained by Gel red (a) and in the presence of compound **1a** (b, 24 μM for lane 1–9 and 11, 12 μM for lane 10) before the electrophoresis. Lane 1: DNA marker; lane 2: hybrid-type G2T1 (6 μM); lane 3: hybrid-type Telo22 (12 μM); lane 4: c-kit1 (12 μM); lane 5: c-kit2 (12 μM); lane 6: VEGF (12 μM); lane 7: KRAS (12 μM); lane 8: bcL-2 (12 μM); lane 9: ds 26 (12 μM); lanes 10 and 11: Pu22 (12 μM), respectively.

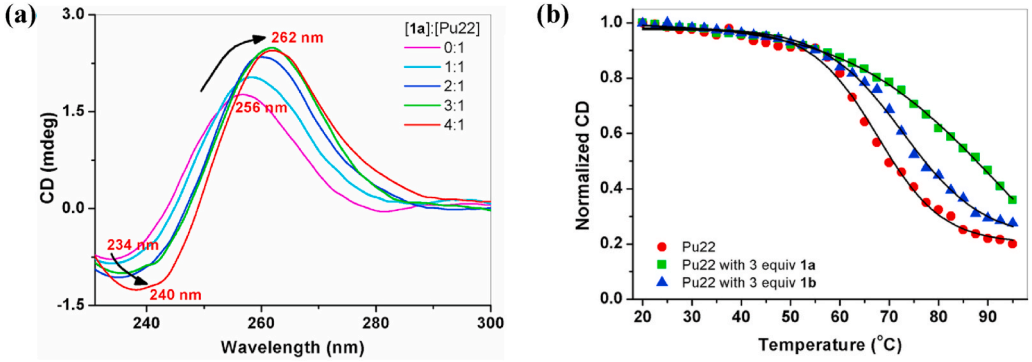

Fig. 3. (a) CD spectra of non-annealed Pu22 (5 μM) in 10 mM Tris-HCl (pH 7.2) buffer in the presence of compound **1a**. (b) CD melting curves for c-myc Pu22 G-quadruplex (5 μM) without and with compounds **1a** and **1b** in 10 mM Tris-HCl buffer (5 mM KCl, 95 mM LiCl and pH 7.2).

The selective fluorescence response of compound **1a** towards c-myc Pu22 G-quadruplex was further visualized by staining different DNA olinucleotides with compound **1a** and Gel red on a native gel (Fig. 2) [30]. At first, Gel red could stain all DNA olinucleotides in Fig. 2a. However, compound **1a** selectively stained certain DNA sequences in Fig. 2b. Compound **1a** could stain c-myc Pu22 G-quadruplex (lanes 10–11, Fig. 2b), even exhibit better dyeing effect than Gel red in the same condition by comparing lane 10 in Fig. 2a with lane 11 in Fig. 2b. And Compound **1a** staining c-myc Pu22 G-quadruplex exhibited concentration dependence (lanes 10–11, Fig. 2b). But the staining of

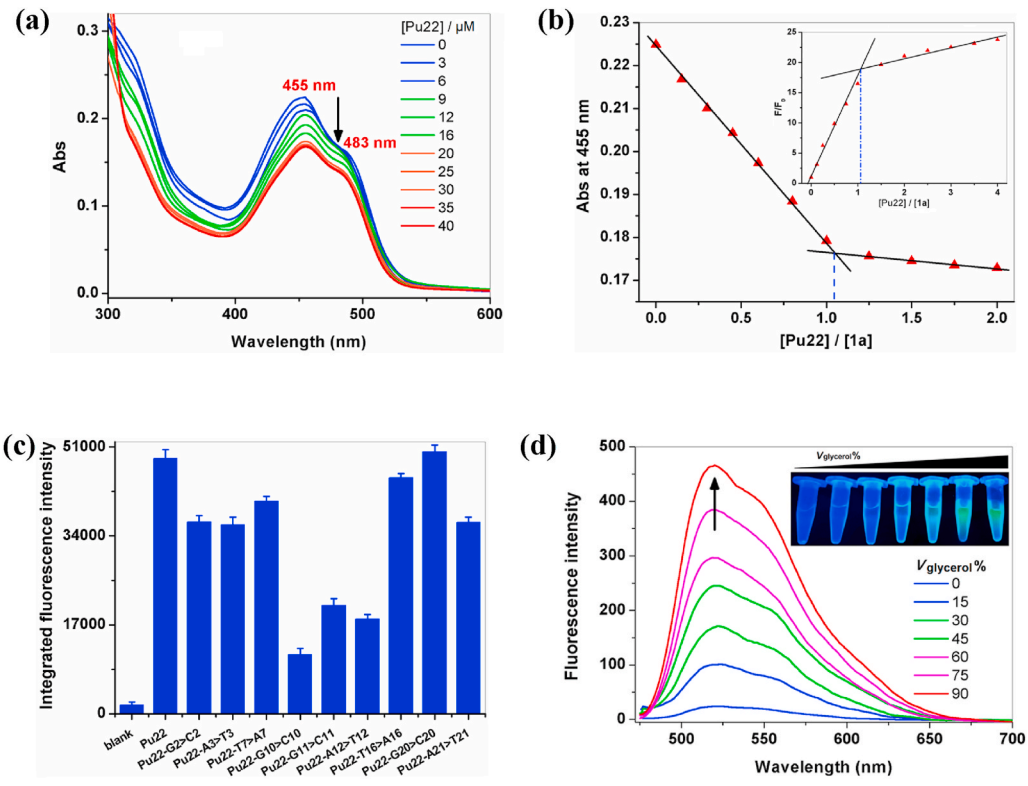

Fig. 4. (a) UV–Vis titration spectra of compound **1a** (20 μM) upon increasing concentration (0–40 μM) of Pu22. (b) Plot of absorbance value at 455 nm of compound **1a** upon increasing concentration of Pu22 *vs* binding ratio of [Pu22]/[**1a**]. Inset: plot of the relative fluorescence intensity F/F_0 at 516 nm of compound **1a** upon increasing concentration of Pu22 *vs* binding ratio of [Pu22]/[**1a**], λ_{ex} = 455 nm. (c) Integrated fluorescence intensity values of compound **1a** (1 μM) at 516 nm without and with 4 μM Pu22 and its mutants. (d) Fluorescence spectra of compound **1a** in aqueous glycerol solution containing different concentrations of glycerol (λ_{ex} = 455 nm), respectively.

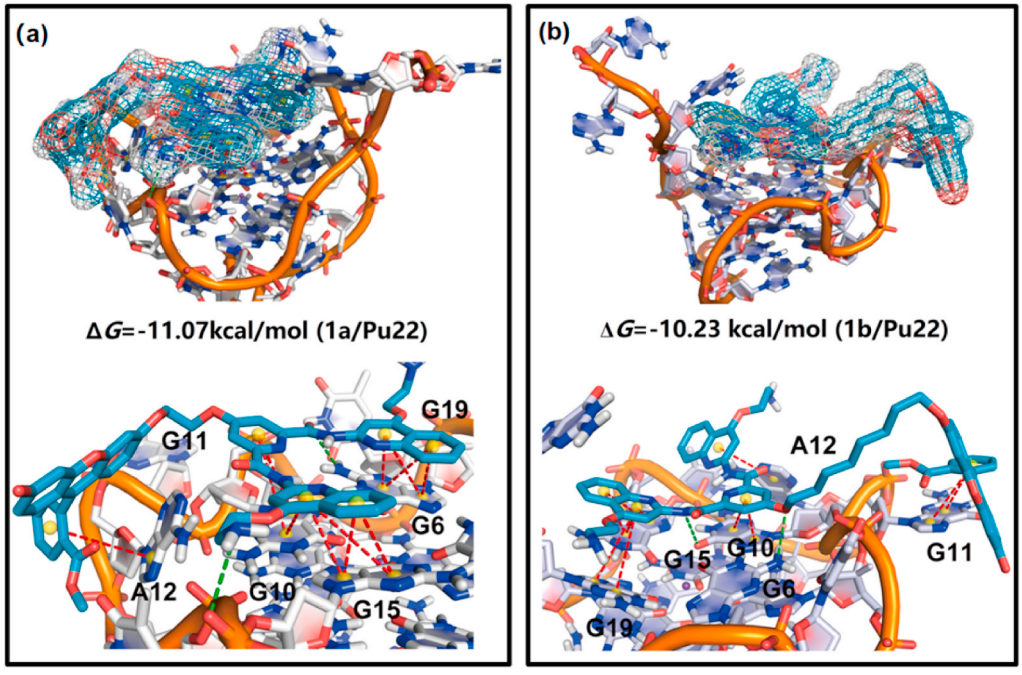

Fig. 5. Molecular modelling of compounds **1a** (a) and **1b** (b) with Pu22.

compound **1a** was weak towards hybrid-type G2T1 (lane 2), hybrid-type Telo22 (lane 3) and c-kit2 (lane 5) in Fig. 2b. And compound **1a** seldom stained c-kit1 (lane 4), VEGF (lane 6), KRAS (lane 7), bcL-2 (lane 8) and ds 26 (lane 9) in Fig. 2b. These results further prove that compound **1a** could selectively detect c-myc Pu22 G-quadruplex.

3.3. Binding affinity towards DNA

The interaction of compounds **1a** and **1b** with different DNA sequences have been analyzed by fluorescence titration assays and their DNA-binding affinities (K_a's) were summarized in Table 3, Figs. S21 and S22. The fluorescence intensity of compound **1a** increased with the concentration of Pu22 (Fig. S21a). The apparent binding constant (K_a) of compound **1a** towards the Pu22 was 6.31 ± 0.84 μM^{-1}. Compound **1a**

Table 4
Comparison of fluorescence recognition between conjugates **1a** and **1b** and the reported G-quadruplex probes of G_4 ligand–linker–fluorophore.

Compound	linker	G-quadruplex	F/F_0 (Φ_F)
Ber-PDS	$-CH_2(CH_2OCH_2)_2CH_2-$	^{Anti} G2T1	186-fold (0.54)
		^{Hybrid} G2T1	58-fold (0.26)
Ber-360A	$-CH_2(CH_2OCH_2)_2CH_2-$	^{Anti} G2T1	83-fold (0.26)
		^{Hybrid} G2T1	40-fold (0.11)
360A-C	$-CH_2(CH_2OCH_2)_2CH_2-$	^{Hybrid} G1	160-fold
		^{Anti} G1	(0.021)
			100-fold (/[a])
CNDI	$-CH_2(CH_2)_5CH_2-$	^{Paral} G1 (c-kit1)	34-fold (/)
		^{Hybrid} G1	17-fold (/)
		^{Anti} G1	15-fold (/)
PDP-Cy5	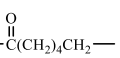	Most $^{hybrid/paral}$ G1	/(/)
SiR-PyPDS	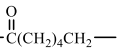	^{Paral} G1 (c-myc)	4-fold (0.2)
IZFL	$-CH_2(CH_2)_2CH_2-$	^{Paral} G1 (c-myc Pu18)	14.2-fold (/)
1a	$-CH_2CH_2-$	^{Paral} G1 (c-myc Pu22)	25-fold (0.67)
1b	$-CH_2(CH_2)_6CH_2-$	^{Paral} G1 (c-myc Pu22)	3.3-fold (0.12)

[a] / = no reported.

showed a 3.7–6.3-fold higher binding affinity for Pu22 than for antiparallel and hybrid-type G2T1, antiparallel Telo22, c-kit1, VEGF, KRAS and bcL-2, respectively. And compound **1a** showed 23.4 and 28.7-fold higher binding affinity for Pu22 than for hybrid-type Telo22 and c-kit2, respectively. Even, compound **1a** showed 485-fold higher binding affinity for Pu22 than ds 26. These results suggest that compound **1a** showed higher binding affinity towards Pu22 than the other G-quadruplexes in human telomere and gene promoter regions and double-stranded DNA. Compared with compound **1b** (Fig. S22), compound **1a** showed 6.3-fold higher binding affinity for Pu22.

3.4. Formation and stabilization towards Pu22

For the formation and stabilization of the G-quadruplexes in the promoter region of the c-myc gene could possibly control the over-expression of the c-myc protein and the transcription of the c-myc oncogene, it is crucial to discuss the effect of compounds **1a** and **1b** on the conformation and thermal stabilization towards Pu22 by CD spectra. Non-annealed Pu22 without potassium, sodium or any compounds showed the characteristic positive ellipticity at *ca.* 256 nm and negative ellipticity at *ca.* 234 nm, which is consistent with a single-stranded DNA sequence (Fig. 3a) [39,51]. Addition of compound **1a** into non-annealed Pu22 caused up to a noticeable redshift from *ca.* 234 nm and 256 nm to *ca.* 240 nm and 262 nm, respectively, while the signals associated to the formation of parallel G-quadruplex (a positive ellipticity at *ca.* 262 nm and a negative ellipticity at *ca.* 240 nm) increased. The result demonstrates that compound **1a** could induce the formation of parallel G-quadruplexes [39,51]. The potential templating effect of compound **1b** towards Pu22 had been also measured. As shown in Fig. S25a, though addition of compound **1b** into non-annealed Pu22 caused up to a redshift from *ca.* 260 nm to *ca.* 263 nm, the CD intensity at *ca.* 263 nm first increased and then decreased with the rise of the concentration of compound **1b**, which might result in aggregation or precipitation of Pu22 [39].

Furthermore, the melting of c-myc Pu22 G-quadruplex was carried out in the presence of compounds **1a** and **1b** by CD-melting. By CD spectra, addition of compounds **1a** and **1b** caused no significant structural changes towards parallel c-myc Pu22 G-quadruplex (Figs. S25b

Table 5
IC_{50} values (μM) of compounds **1a** and **1b** against a panel of cell lines.

Compound	IC_{50} (μM)		
	A549	MCF-7	HeLa
1a	11.9 ± 0.9	14.4 ± 1.2	18.0 ± 1.3
1b	33.7 ± 2.2	28.9 ± 0.2	54.1 ± 4.2

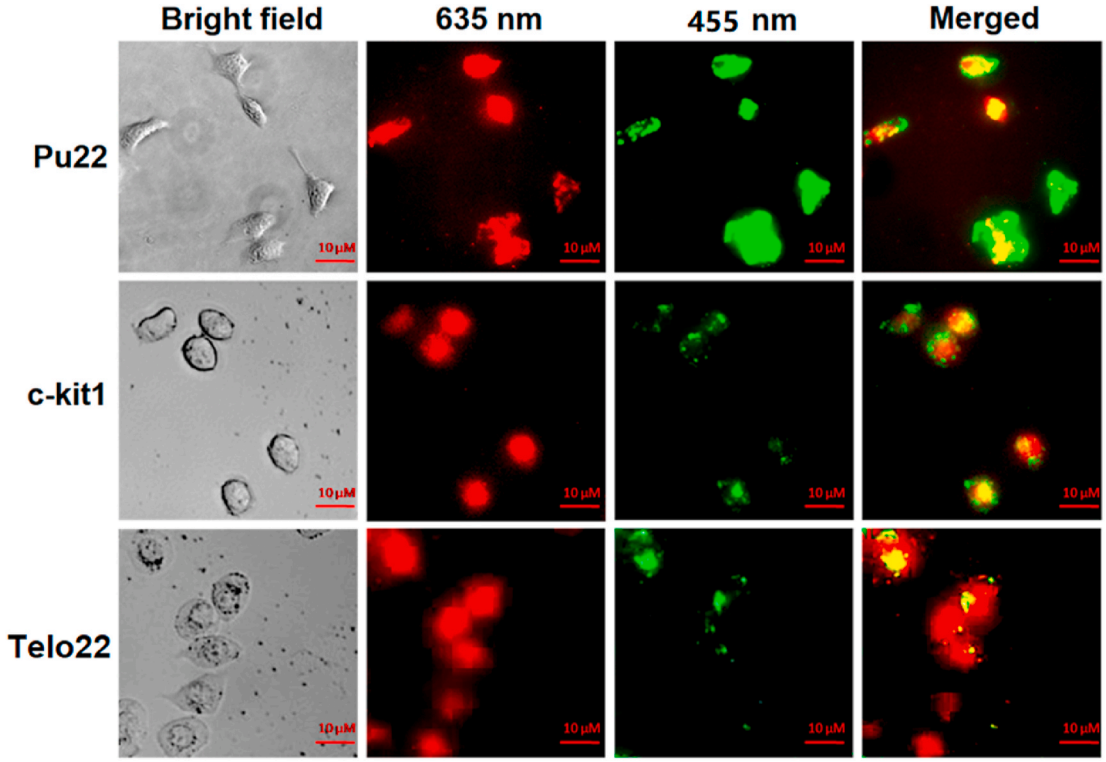

Fig. 6. Microscopy images of MCF-7 cells transfected by 5′-Cy5-Pu22, 5′-Cy5-c-kit1 and 5′-Cy5-Telo22 and incubated by compound **1a** (5 μM).

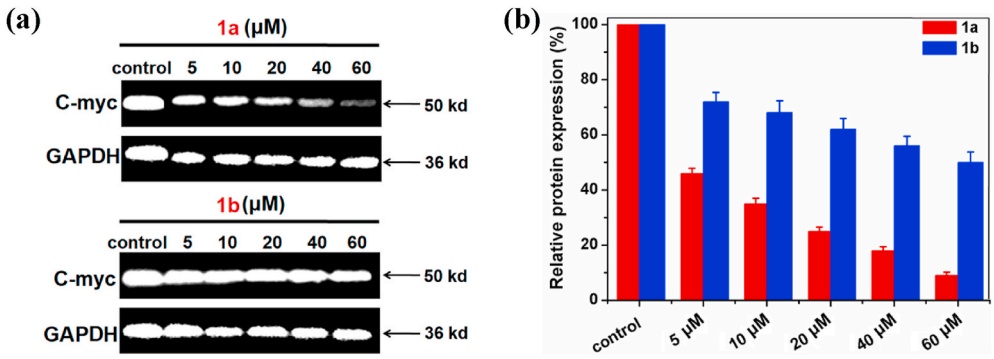

Fig. 7. (a) Immunoreactive bands of the c-myc protein in A549 cells were analyzed by western blotting in the absence and presence of compounds **1a** and **1b**. (b) Densitometric analyses of immunoblots upon treatment with compounds **1a** and **1b.**

and S25c). As shown in Fig. 3b, compound **1a** showed good thermal stabilization towards Pu22 (ΔT_m = 16.1 ± 0.4 °C), and also exhibited higher thermal stabilization than compound **1b** (ΔT_m = 6.5 ± 0.5 °C). As shown in Table 3, compound **1a** showed a very little effect on the T_m of gene promoter G-quadruplexes including c-kit1, c-kit2, KRAS, VEGF and bcL-2, respectively (Fig. S27), and also showed low thermal stabilization towards human telomeric G-quadruplexes (Fig. S28a~d) and ds 26 (Fig. S28e). These results suggest that compound **1a** exhibited higher thermal stabilization towards c-myc Pu22 G-quadruplex than other G-quadruplexes and double-stranded DNA.

3.5. *Binding site analysis and fluorescence mechanism*

Compared with conjugate **1b** with longer alkyl linker, conjugate **1a** with shorter alkyl linker exhibited higher fluorescence response, binding affinity and thermal stabilization towards c-myc Pu22 G-quadruplex than other G-quadruplexes in human telomere and gene promoter regions and double-stranded DNA. Binding site analysis will help to find out the reason that compound **1a** could show higher selectivity and fluorescence response towards Pu22 by experimental assays and molecule modelling.

At first, the binding modes were analyzed by UV–Vis titrations, fluorescence titrations and CD spectra. In the Tris-HCl buffer, **PDS** (λ_{max} = 269 nm, ε = 21, 900 M^{-1} cm^{-1}) and fluorescein derivative **2** (Scheme 2) had some absorbance peaks below 350 nm. However, above 350 nm, only fluorescein portion had two absorbance peaks at 459 nm (ε = 23, 162 M^{-1} cm^{-1}) and 498 nm (ε = 29, 044 M^{-1} cm^{-1}). For fluorescein chromophore was conjugated with PDS in compound **1a**, these two absorbance peaks of fluorescein portion blueshifted to 455 nm (ε = 11, 245 M^{-1} cm^{-1}) and 483 nm (ε = 8, 283 M^{-1} cm^{-1}) and caused 55.5% and 72.1% hypochromicity, respectively (Fig. S24b). And these two absorbance peaks of fluorescein portion in compound **1b** resulted in a slightly lower hypochromicity (50.4% at 459 nm (ε = 11, 300 M^{-1} cm^{-1}) and 64.1% at 486 nm (ε = 10, 301 M^{-1} cm^{-1}), respectively) than those in compound **1a** (Fig. S24b). These results suggest that the stronger interaction between two moieties of conjugate **1a** promoted the conformational change of fluorescein chromophore and resulted in stronger the fluorescence quenching than that of conjugate **1b** in Tris-HCl buffer (Fig. S24c). Upon addition of Pu22, these two absorbance peaks of fluorescein portion in compound **1a** caused 25.4% and 17.1% hypochromicity at *ca.* 455 nm and 483 nm, respectively, but did not appear a remarkable redshift at these two peaks (Fig. 4a). For the noticeable redshift at above 300 nm suggested a π-π stacking with G-tetrad [38,39,51], no redshift suggests that the fluorescein portion did not bind with Pu22 by π-π stacking with G-tetrad. No positive/negative ICD bands above 300 nm (Fig. S25d) further indicates that the binding of the fluorescein portion towards Pu22 was neither end-stacking with G-tetrad nor an intercalation [52]. As a comparative study, these two absorbance peaks of fluorescein portion in compound **1b** caused 9.5% and 9.2% hyperchromicities at *ca.* 459 nm and 492 nm, respectively, and also had no redshift (Fig. S24d). In addition, the results of UV–Vis and fluorescence titrations suggest a 1:1 binding ratio between compound **1a** and Pu22 in Fig. 4b.

Furthermore, fluorescence alterations upon recognition between compound **1a** and the mutant c-myc Pu22 G-quadruplex sequences (Table 2 and Scheme 1c) were analyzed to investigate the binding site of compound **1a** [27,30]. The oligonucleotides mutated at the 5′-overhang (Pu22-G2>C2 and Pu22-A3>T3), the 1st loop (Pu22-T7>A7), the 2nd loop (Pu22-G11>C11 and Pu22-A12>T12), the 3rd loop (Pu22-T16>A16), 3′-overhang (Pu22-G20>C20 and Pu22-A21>T21) and 3′-end G-quartet (Pu22-G10>C10), respectively. The CD spectra show that these mutated DNA oligonucleotides formed the same topology as c-myc Pu22 G-quadruplex and addition of compound **1a** did not change their topology (Fig. S26). Upon addition of compound **1a**, oligonucleotides with mutation at 5′-overhang (Pu22-G2>C2 and Pu22-A3>T3), the 1st loop (Pu22-T7>A7), the 3rd loop (Pu22-T16>A16) and 3′-end loop (Pu22-A21>T21) exhibited strong fluorescence response like the native Pu22 (Fig. 4c and S23). And 3′-overhang (Pu22-G20>C20) exhibited lightly higher fluorescence response than the native Pu22 (Fig. 4c). These results suggest that compound **1a** did not or slightly bind on the 5′-end G-quartet, the 5′-overhang, the 1st loop, the 3rd loop and 3′-overhang. Instead, compound **1a** for the oligonucleotides mutated at 3′-end G-quartet (Pu22-G10>C10) and the 2nd loop (Pu22-G11>C11 and Pu22-A12>T12) showed the weak fluorescence response (Fig. 4c), which indicates that compound **1a** might be located on the 3′-end G-quartet and the 2nd loop [27,30]. Combined with the result of a 1:1 binding ratio between compound **1a** and Pu22, one molecule of compound **1a** possibly located on the 3′-end G-quartet and the 2nd loop of one Pu22 G-quadruplex molecule.

On base of the above experimental results, the more concrete binding mode between compound **1a** and c-myc Pu22 G-quadruplexes had been discussed by molecular modeling in Fig. 5a. **PDS**, as an excellent G-quadruplex binder, had been reported that an optimal electronic density of the aromatic surface made it enable π-π interaction with G-tetrad [42,53]. Thus, the bisquinolinium portion of one molecule **1a** stacked on 3′-end G-quartet corresponding to the base G10 according to the result of fluorescence alterations upon recognition. And the fluorescein portion of this molecule **1a** did not stack on 3′-end G-quartet, but bound on the 2nd loop corresponding to the bases G11 and A12 according to the results of UV–Vis titration, ICD and fluorescence alterations upon recognition. As a comparative study, though the bisquinolinium portion of one **1b** also bound on 3′-end G-quartet, the fluorescein portion only slightly bound on the base of G11 and seldom bound on the base of A12 in the 2nd loop due to its longer alkyl linker (Fig. 5b). In addition, compound **1a** exhibited higher binding affinity towards c-myc Pu22 G-quadruplex than compound **1b** (−11.07 kcal mol^{-1} for **1a** and −10.23 kcal mol^{-1} for **1b**, respectively), which is also consistent with

the K_a values. These results indicate that the regulation of alkyl linker played an important role in the binding affinity of compound **1a** towards Pu22.

Luminescent mechanism of compound **1a** towards Pu22 had been further analyzed. According to the result of the experimental data and molecule modelling, the binding of fluorescein portion on the 2nd loop of Pu22 prevented fluorescein plane rotation and induced to the fluorescence light-up of compound **1a** [37–39]. The viscosity experiment had proved this hypothesis. With the rise of the content of glycerol in the glycerol-water solution, the viscosity increased and compound **1a** exhibited significant increase on the fluorescence intensity at *ca.* 516 nm in Fig. 4d. The increase of the viscosity prevented the fluorescein plane rotation, resulted in the conformational changes in the excited state of fluorescein plane, and excited the fluorescence of compound **1a**.

3.6. Fluorescence response comparison with the reported G-quadruplex probes of G_4 ligand–linker–fluorophore

To find out some rules to design the probes selectively recognizing parallel c-myc G-quadruplexes, we have analyzed and compared the fluorescence recognition of the reported conjugates of G-quadruplex binder and fluorophore ligand with the polyether or alkyl chains towards G-quadruplexes with different confirmations (Table 4). The conjugates with the polyether linkers (**Ber-PDS**, **Ber-360A** and **360A-C**, Scheme 1a) exhibited higher fluorescence response towards antiparallel and hybrid-type G-quadruplexes than parallel G-quadruplexes [34,39]. The conjugates with the alkyl linkers (**CNDI**, **PDY-Cy5**, **SiR-PyPDS, IZFL** and **1a**, Schemes 1a~b) exhibited high fluorescence response towards parallel and hybrid-type G-quadruplexes, especially parallel G-quadruplexes [35,36,40,41]. Significantly, compared with compound **PDP-Cy5** with longer alkyl linker, which exhibited fluorescence response towards most hybrid-type and parallel G-quadruplex DNA and RNA, compound **1a** with the shorter alkyl linker only exhibited high fluorescence response towards parallel c-myc Pu22 G-quadruplex. These comparisons indicate that a conjugate of G-quadruplex binder and fluorescence ligand with the alkyl linker could more likely realize the fluorescence response towards parallel G-quadruplexes. Furthermore, the regulation of the length of alkyl linker like **IZFL** and **1a** could be expected to selectively recognize parallel c-myc G-quadruplexes. The possible reason will be further discussed in the future.

3.7. Cell imaging of compound *1a* with c-myc Pu22 G-quadruplex

Encouraged by the result of fluorescence response towards c-myc Pu22 G-quadruplex, the co-localization of compound **1a** and c-myc Pu22 G-quadruplex in cells was investigated to determine whether **1a** could selectively recognize c-myc Pu22 G-quadruplex in cells [30,35]. At first, c-myc Pu22 G-quadruplex labeled with 5′-Cy5 (5′-Cy5-Pu22, Table 1) was transfected into MCF-7 cells with lipofectamine 2000. After the cells were incubated with compound **1a**, red fluorescence signals explored the distribution of c-myc Pu22 in the cells upon the excitation of Cy5 at λ_{ex} = 635 nm (Fig. 6). At λ_{ex} = 455 nm, the binding of compound **1a** towards c-myc Pu22 resulted in strong green fluorescence signals in the cells. Obviously, most green fluorescence signals were co-localized with red fluorescence signals, which suggests the recognition of compound **1a** towards c-myc Pu22 G-quadruplex in cells [30,35]. As a comparative study, the co-localization of compound **1a** towards human telomerase G-quadruplex Telo22 labeled with 5′-Cy5 (5′-Cy5-Telo22, Table 1) or c-kit1 G-quadruplex labeled with 5′-Cy5 (5′-Cy5-c-kit1, Table 1) in MCF-7 cells were also investigated. Similarly, red fluorescence signals explored the distribution of Telo22 and c-kit1 in the cells at λ_{ex} = 635 nm (Fig. 6). However, addition of compound **1a** only caused few green fluorescence signals and little co-localization between Telo22 or c-kit1 and **1a** (Fig. 6). These results indicate that compound **1a** exhibited higher fluorescence response towards c-myc Pu22 than Telo22 and c-kit1 in cells, and selectively recognized c-myc Pu22 G-quadruplex in MCF-7 cells. Furthermore, the above result had been proved in A549 cells (Fig. S29).

3.8. Cytotoxicity and regulation of c-myc expression

The above results suggest that compound **1a** induced the formation of c-myc Pu22 G-quadruplex, and showed high binding affinity and selectivity towards c-myc Pu22 both in vitro and in cells. For targeting the G-quadruplexes in the c-myc gene region could possibly inhibit the proliferation of cancer cells, the cytotoxicity of compounds **1a** and **1b** towards three cancerous cell lines (i.e. A549, MCF-7 and HeLa, respectively) had been evaluated in Table 5 with the MTT assay. Compound **1a** exhibited higher inhibitory activities against three cancer cells than compound **1b**, which is possibly related to the selective binding of compound **1a** towards c-myc G-quadruplex in cells.

Thus, to evaluate the inhibitory abilities of compounds **1a** and **1b** on the expression of c-myc, western blot assays were carried out using A549 cells [14,27,49]. A549 cells were treated with compounds **1a** and **1b** and then the total c-myc protein levels were quantified relative to the expression of GAPDH as the house-keeping gene. As shown in Fig. 7, c-myc protein expression significantly decreased in the presence of compound **1a**. However, c-myc protein expression only showed a weak decrease in the presence of compound **1b**. These results further suggest that the compound **1a** might target c-myc G-quadruplex in cancer cells, downregulate the c-myc protein and inhibit the proliferation of cancer cells.

4. Conclusions

In summary, two novel bisquinolinium-fluorescein conjugates (**1a** and **1b**) tethered by different-length alkyl linkers have been designed and synthesized. Their fluorescence response, binding selectivity and thermal stabilization for c-myc Pu22 G-quadruplex have been discussed by spectrometric titrations, electrophoresis, CD spectroscopy and CD-melting. Compared with conjugate **1b** with longer alkyl linker, conjugate **1a** with shorter alkyl linker, exhibited higher fluorescence response, binding and thermal stabilization towards c-myc Pu22 G-quadruplex from human telomere G-quadruplexes, other G-quadruplexes in the promoter regions and double-stranded DNA. According to the study of binding modes, the bisquinolinium portion of one molecule **1a** stacked on 3′-end G-quartet, and the fluorescein portion bound on the 2nd loop, which increases the selectivity and excites the fluorescence towards Pu22. Furthermore, conjugate **1a** exhibited a specific recognition towards c-myc Pu22 G-quadruplex DNA in cells through microscopy experiments. In addition, compound **1a** showed potential anticancer activity. Western blot assay further proved that compound **1a** could inhibit cell proliferation possibly by reducing c-myc expression.

Overall, the alkyl linker between an optical tag and a G-quadruplex binder in the conjugate will give more possibility for recognizing parallel G-quadruplex structures in vitro and in vivo. Furthermore, the regulation of the length of the alkyl linker played a significant role in the selectivity towards parallel c-myc G-quadruplexes. This study provides guidance to design the high-performance fluorescence probes towards c-myc G-quadrulexes, and develop anticancer drugs targeting c-myc G-quadruplexes.

CRediT authorship contribution statement

Jun-Hui Li: Investigation and writing - original draft. **Tian-Zhu Ma**, **Jia-Luo Fu**, **Jun-Tao Huang**, **Meng-Jia Zhang** and **Pei-Dan You:** Investigation. **Chun-Qiong Zhou:** Writing - review & editing.

Declaration of competing interest

The authors declare that they have no known competing financial

interests or personal relationships that could have appeared to influence the work reported in this paper.

Acknowledgement

This work was financially supported by Guangdong Science and Technology Department of China (2017A050501018) and Southern Medical University (YD2017N001).

Appendix A. Supplementary data

Supplementary data to this article can be found online at https://doi.org/10.1016/j.dyepig.2021.109304.

References

[1] Seimiya H. Crossroads of telomere biology and anticancer drug discovery. Canc Sci 2020;111:3089–99.
[2] Wang W, Hu S, Gu Y, Yan Y, Stovall DB, Li D, Sui G. Human MYC G-quadruplex: from discovery to a cancer therapeutic target. BBA-Rev Canc 2020;1874:188410.
[3] Rigo R, Dean WL, Gray RD, Chaires JB, Sissi C. Conformation profiling of a G-rich sequence with the c-KIT promoter. Nucleic Acids Res 2017;45:13056–67.
[4] Cogoi S, Ferino A, Miglietta G, Pedersen EB, Xodo LE. The regulatory G4 motif of the Kirsten ras (KRAS) gene is sensitive to guanine oxidation: implications on transcription. Nucleic Acids Res 2018;46:661–76.
[5] Onel B, Carver M, Wu G, Timonina D, Kalarn S, Larriva M, Yang D. A new G-quadruplex with hairpin loop immediately upstream of the human BCL2 P1 promoter modulates transcription. J Am Chem Soc 2016;138:2563–70.
[6] Salvati E, Zizza P, Rizzo A, Pagano B, Novellino E. Evidence for G-quadruplex in the promoter of vegfr-2 and its targeting to inhibit tumor angiogenesis. Nucleic Acids Res 2014;42:2945–57.
[7] Siddiqui-Jain A, Grand CL, Bearss DJ, Hurley LH. Direct evidence for a G-quadruplex in a promoter region and its targeting with a small molecule to repress c-MYC transcription. Proc Natl Acad Sci U S A 2002;99:11593–8.
[8] Whitfield JR, Beaulieu ME, Soucek L. Strategies to inhibit Myc and their clinical applicability. Front. Cell Dev. Biol. 2017;5:10.
[9] Ambrus A, Chen D, Dai J, Jones RA, Yang D. Solution structure of the biologically relevant G-quadruplex element in the human c-MYC promoter. Implication for G-quadruplex stabilization. Biochemistry 2005;44:2048–58.
[10] Dang CV. C-myc target genes involved in cell growth, apoptosis, and metabolism. Mol Cell Biol 1999;19:1–11.
[11] Collie GW, Parkinson GN. The application of DNA and RNA G-quadruplexes to therapeutic medicines. Chem Soc Rev 2011;40:5867–92.
[12] Wei ZZ, Qin QP, Meng T, Deng CX, Liang H, Chen ZF. 5-Bromo-oxoisoaporphine platinum(II) complexes exhibit tumor cell cytotoxicity via inhibition of telomerase activity and disruption of c-myc G-quadruplex DNA and mitochondrial functions. Eur J Med Chem 2018;145:360–9.
[13] Qin JL, Qin QP, Wei ZZ, Yu YC, Meng T, Wu CX, Liang YL, Liang H, Chen ZF. Stabilization of c-myc G-quadruplex DNA, inhibition of telomerase activity, disruption of mitochondrial functions and tumor cell apoptosis by platinum(II) complex with 9-amino-oxoisoaporphine. Eur J Med Chem 2016;124:417–27.
[14] Zhang S, Wu Q, Zhang H, Wang Q, Wang X, Mei W, Wu X, Zheng W. Microwave-assisted synthesis of ruthenium(II) complexes with alkynes as potential inhibitor by selectively recognizing c-myc G-quadruplex DNA. J Inorg Biochem 2017;176:113–22.
[15] Zhang Z, Mei W, Wu X, Wang X, Wang B, Chen S. Synthesis and characterization of chiral ruthenium(II) complexes Λ/Δ-[Ru(bpy)$_2$(H$_2$iip)](ClO$_4$)$_2$ as stabilizers of c-myc G-quadruplex DNA. J Coord Chem 2015;68:1465–75.
[16] Yang H, Ma VPY, Chan DSH, He HZ, Leung CH, Ma DL. A cyclometallated iridium (III) complex as a c-myc G-quadruplex stabilizer and down-regulator of c-myc oncogene expression. Curr Med Chem 2013;20:576–82.
[17] Wu Q, Song Y, Liu R, Wang R, Mei W, Chen W, Yang H, Wang X, Synthesis. Docking studies and antitumor activity of phenanthroimidazole derivatives as promising c-myc G-quadruplex DNA stabilizers. Bioorg Chem 2020;102:104074.
[18] Liu HY, Chen AY, Yin QK, Li Z, Huang SM, Du G, He JH, Zan LP, Wang SK, Xu YH. New disubstituted quindoline derivatives inhibiting burkitt's lymphoma cell proliferation by impeding c-MYC transcription. J Med Chem 2017;60:5438–54.
[19] Jiang Y, Chen AC, Kuang GT, Wang SK, Ou TM, Tan JH, Li D, Huang ZS. Design, synthesis and biological evaluation of 4-anilinoquinazoline derivatives as new c-myc G-quadruplex ligands. Eur J Med Chem 2016;122:264–79.
[20] Liao SR, Zhou CX, Wu WB, Ou TM, Tan JH, Li D, Gu LQ, Huang ZS. 12-N-methylated 5, 6-dihydrobenzo[c]acridine derivatives: a new class of highly selective ligands for c-myc G-quadruplex DNA. Eur J Med Chem 2012;53:52–63.
[21] Seenisamy J, Bashyam S, Gokhale V, Vankayalapati H, Sun D, Siddiqui-Jain A, Streiner N, Shinya K, White E, Wilson WD. Design and synthesis of an expanded porphyrin that has selectivity for the c-MYC G-quadruplex structure. J Am Chem Soc 2005;127:2944–59.
[22] Tawani A, Mishra SK, Kumar A. Structural insight for the recognition of G-quadruplex structure at human c-myc promoter sequence by flavonoid quercetin. Sci Rep 2017;7:1–13.
[23] Lee HM, Chan DSH, Yang F, Lam HY, Yan SC, Che CM, Ma DL, Leung CH. Identification of natural product fonsecin B as a stabilizing ligand of c-myc G-quadruplex DNA by high throughput virtual screening. Chem Commun 2010;46:4680–2.
[24] Dutta D, Debnath M, Muller D, Paul R, Das T, Bessi I, Schwalbe H, Dash J. Cell penetrating thiazole peptides inhibit c-MYC expression via site-specific targeting of c-MYC G-quadruplex. Nucleic Acids Res 2018;46:5355–65.
[25] Deianan M, Chand K, Jamroskovic J, Das RN, Obi I, Chorell E, Sabouri N. A site-specific self-assembled light-up rotor probe for selective recognition and stabilization of c-MYC G-quadruplex DNA. Nanoscale 2020;12:12950–7.
[26] Wang MQ, Zhang Y, Zeng XY, Yang H, Yang C, Fu RY, Li HJ. A benzo(f)quinolinium fused chromophore-based fluorescent probe for selective detection of c-myc G-quadruplex DNA with a red emission and a large stocks shift. Dyes Pigments 2019;168:334–40.
[27] Hu MH, Wang YQ, Yu ZY, Hu LN, Ou TM, Chen SB, Huang ZS, Tan JH. Discovery of a new four-leaf clover-like ligand as a potent c-MYC transcription inhibitor specifically targeting the promoter G-quadruplex. J Med Chem 2018;61:2447–59.
[28] Chauhan A, Paul R, Debnath M, Bessi I, Mandal S, Schwalbe H, Dash J. Synthesis of fluorescenct binaphthyl amines that bind c-MYC G-quadruplex DNA and repress c-MYC expression. J Med Chem 2016;59:7275–81.
[29] Kumar YP, Bhowmik S, Das RN, Bessi I, Paladhi S, Ghosh R, Schwalbe H, Dash J. A fluorescent guanosine dinucleoside as a selective switch-on sensor for c-myc G-quadruplex DNA with potent anticancer activities. Chem Eur J 2013;19:11502–6.
[30] Zhai Q, Gao C, Ding J, Zhang Y, Islam B, Lan W, Hou H, Deng H, Li J, Hu Z, Mohamed HI, Xu S, Cao C, Haider SM, Wei D. Selective recognition of c-MYC Pu22 G-quadruplex by a fluorescent probe. Nucleic Acids Res 2019;47:2190–204.
[31] Chen SB, Wu WB, Hu MH, Ou TM, Gu LQ, Tan JH, Huang ZS. Discovery of a new fluorescent light-up probe specific to parallel G-quadruplexes. Chem Commun 2014;50:12173–6.
[32] Lu YJ, Yan SC, Chan FY, Zou L, Chung WH, Wong WL, Qiu B, Sun N, Chan PH, Huang ZS. Benzothiazole-substituted benzofuroquinolinium dye: a selective switch-on fluorescent probe for G-quadruplex. Chem Commun 2011;47:4971–3.
[33] Lin D, Fei X, Gu Y, Wang C, Tang Y, Li R, Zhou J. A benzindole substituted carbazole cyanine dye: a novel targeting fluorescent probe for parallel c-myc G-quadruplexes. Analyst 2015;140:5772–80.
[34] Xie X, Reznichenko O, Chaput L, Martin P, Teulade-Fichou MP, Granzhan A. Topology-selective, fluorescent "light-up" probes for G-quadruplex DNA based on photoinduced electron transfer. Chem Eur J 2018;24:12638–3651.
[35] Wu F, Liu C, Chen Y, Yang S, Xu J, Huang R, Wang X, Li M, Liu W, Mao W, Zhou X. Visualization of G-quadruplexes in gel and in live cells by a near-infrared fluorescent probe. Sensor Actuator B Chem 2016;236:268–75.
[36] Hu MH, Zhou J, Luo WH, Chen SB, Huang ZS, Wu R, Tan JH. Development of a smart fluorescent sensor that specifically recognizes the c-MYC G-quadruplex. Anal Chem 2019;91:2480–9.
[37] Zhou CQ, Yang JW, Dong C, Wang YM, Sun B, Chen JX, Xu YS, Chen WH. Highly selective, sensitive and fluorescent sensing of dimeric G-quadruplexes by a dimeric berberine. Org Biomol Chem 2016;14:191–7.
[38] Li ZQ, Liao TQ, Dong C, Yang JW, Chen XJ, Liu L, Luo Y, Liang YY, Chen WH, Zhou CQ. Specifically targeting hybrid-type dimeric G-quadruplexes using berberine dimmers. Org Biomol Chem 2017;15:10221–9.
[39] Liao TC, MaTZ, Chen SB, Cilibrizzi A, Zhang MJ, Li JH, Zhou CQ. Human telomere double G-quadruplex recognition by berberine-bisquinolinium imaging conjugates in vitro and in cells. Int J Biol Macromol 2020;158:1299–309.
[40] Antonio Di A, Ronjavic A, Radzevičius A, Ranasinghe TR, Catalano M, Zhang X, Shen J, Needham L, Lee SF, Klenerman D, Balasubramanian S. Single-molecule visualization of DNA G-quadruplex formation in live cells. Nat Chem 2020;12:832–7.
[41] Zuffo M, Doria F, Spalluto V, Ladame S, Freccero M. Red/NIR G-quadruplex sensing, harvesting blue light by a coumarin-naphthalene diimide dyad. Chem Eur J 2015;21:17596–600.
[42] Müller S, Sanders DA, MDi Antonio, Matsis S, Riou JF, Rodriguezz R, Balasubramanian S. Pyridostatin analogues promote telomere dysfunction and long-term growth inhibition in human cancer cells. Org Biomol Chem 2012;10:6537–46.
[43] Moruno-Manchon JF, Koellhoffer EC, Gopakumar J, Hamborole S, Kim N, McCullough LD, Tsvetkov AS. The G-quadruplex DNA stabilizing drug pyridostatin promotes DNA damage and downregulates transcription of Brca1 in neurons. Aging 2017;9:1957–70.
[44] Zimmer J, Tacconi EMC, Folio C, Badie S, Porru M, Klare K, Tumiati M, Markkanen E, Halder S, Ryan A, Jackson SP, Ramadan K, Kuznestsov SG, Biroccio A, Sale JE, Tarsounas M. Targeting BRCA1 and BRCA2 deficiencies with G-quadruplex-interacting compounds. Mol Cell 2016;61:1–12.
[45] Jin B, Zhang X, Zheng W, Liu X, Zhou J, Zhang N, Wang F, Shangguan D. Dicyanomethylene-functionalized squaraine as a highly selective probe for parallel G-quadruplexes. Anal Chem 2014;86:7063–70.
[46] Fleming GR, Knight WE, Morris JM, Morrison RJS, Robinon GW. Picosencond fluorescence studies of xanthenes dyes. J Am Chem Soc 1977;99:4306–11.
[47] Pettersen EF, Goddard TD, Huang CC, Couch GS, Greenblatt DM, Meng EC, Ferrin TE. UCSF Chimera-a visualization system for exploratory research and analysis. J Comput Chem 2004;13:1605–12.
[48] Liao GL, Chen X, Wu JH, Qian C, Wang Y, Ji LN, Chao H. Ruthenium(II) polypyridyl complexes as dual inhibitors of telomerase and topoisomerase. Dalton Trans 2015;44:15145–56.
[49] Chauhan A, Paladhi S, Debnath M, Dash J. Selective recognition of c-MYC G-quadruplex DNA using prolinamide derivatives. Org Biomol Chem 2016;14:5761–7.

[50] Minus MB, Kang MK, Knudsen SE, Liu W, Krueger MJ, Smith ML, Redell MS, Ball ZT. Assessing the intracellular fate of rhodium(II) complexes. Chem Commun 2016;52:11685–8.
[51] Liao TC, Ma TZ, Liang Z, Zhang XT, Luo CY, Liu L, Zhou CQ. A comparative study on high selectivities of human telomeric dimeric G-quadruplexes by dimeric G-quadruplex binders. Chem Eur J 2018;24:15840–51.
[52] Mohanty J, Barooah N, Dhamodharan V, Harikrishna S, Pradeepkumar PI, Bhasikuttan AC. Thioflavin T as an efficient inducer and selective fluorescent sensor for the human telomeric G-quadruplex DNA. J Am Chem Soc 2013;135:367–76.
[53] Bugaut A, Rodriguez R, Kumari S, Hsu TD, Balasubramanian S. Small molecule-mediated inhibition of translation by targeting a native RNA G-quadruplex. Org Biomol Chem 2010;8:2771–6.